

Stability, electronic, and optical properties of lead-free halide double perovskites $(\text{CH}_3\text{NH}_3)_2\text{InBiX}_6$ ($X = \text{halogen}$)

Xin Huang^{1,*}, Yunhui Wang¹, Yakui Weng¹, Zhihong Yang^{1,†} and Shuai Dong²

¹New Energy Technology Engineering Laboratory of Jiangsu Province, Information Physics Research Center, School of Science, Nanjing University of Posts and Telecommunications, Nanjing 210023, China

²School of Physics, Southeast University, Nanjing 211189, China

 (Received 24 April 2020; revised 24 August 2020; accepted 8 September 2020; published 12 October 2020)

Recently developed halide double perovskites $A_2M^+M^{3+}X_6$ have attracted attention as potential lead-free perovskite solar cell absorbers. Here, the stability, electronic, and optical properties of the lead-free inorganic-organic hybrid double perovskites $(\text{CH}_3\text{NH}_3)_2\text{InBiX}_6$ ($X = \text{halogen}$) are studied based on density functional theory. By investigating the thermodynamic stability against decomposition, the $(\text{CH}_3\text{NH}_3)_2\text{InBiX}_6$ double perovskites are shown to be stable. Furthermore, the use of a small magnitude of hydrostatic pressure is proposed to improve the thermodynamic stability of double perovskites $(\text{CH}_3\text{NH}_3)_2\text{InBiX}_6$. Meanwhile, the calculated electronic band structures of $(\text{CH}_3\text{NH}_3)_2\text{InBiX}_6$ double perovskites exhibit suitable direct band gaps, small carrier effective masses, and three-dimensional electronic dimensionality. This, in turn, leads to strong optical absorption. Both the electronic and optical features make double perovskites $(\text{CH}_3\text{NH}_3)_2\text{InBiX}_6$ suitable for applications in optoelectronics.

DOI: [10.1103/PhysRevMaterials.4.104601](https://doi.org/10.1103/PhysRevMaterials.4.104601)

I. INTRODUCTION

Hybrid organic-inorganic lead (Pb) halide perovskite APbX_3 ($A = \text{monovalent cations such as Cs or methylammonium}$; $X = \text{I, Br, Cl}$) solar cells have attracted remarkable attention, owing to their dramatic improvement in the record power conversion efficiency (PCE) over the last decade [1,2]. Despite the demonstration of great prospects, the eventual commercialization of such emerging technology is still challenging due to poor long-term stability and Pb-related environmental toxicity. Therefore, tremendous efforts have been committed to the development of nontoxicity and air-stable perovskite-based alternatives [3–7]. Theoretical studies have indicated that the superior photovoltaic properties of lead halide perovskites are mainly attributed to the three-dimensional (3D) electronic dimensionality linked with the high symmetry of the perovskite structure, and the unique electronic configuration of Pb $6s^26p^0$ [3,8,9]. Hence, the straightforward approach to replace Pb^{2+} is to employ similar divalent lone-pair cations Ge^{2+} and Sn^{2+} . However, both Ge and Sn halides suffer from instability issues because Ge and Sn prefer the +4 oxidation state [10,11]. Hence, Ge halides have not fabricated desired solar cells (PCEs < 8%) and Sn-based solar cells generally exhibit PCEs of less than 13%. On the other hand, trivalent lone-pair cations $\text{Sb}^{3+}/\text{Bi}^{3+}$ have also been employed to replace Pb^{2+} , resulting in the low-dimensional perovskite $\text{A}_3(\text{Sb}^{3+}/\text{Bi}^{3+})_2\text{X}_9$ or even non-perovskite compounds [12]. However, it is found that these compounds show undesired optoelectronic properties due to

the unfavored low dimensionality of both crystal and electronic structures [13,14].

Alternatively, the novel 3D halide double perovskite $\text{A}_2M^+M^{3+}X_6$ has been reported, derived by substituting two divalent Pb^{2+} ions in APbX_3 by one trivalent ion M^{3+} and one monovalent ion M^+ [15]. Numerous combinations of elements for M^+ and M^{3+} greatly broaden the exploration range for optoelectronic materials; this strategy of lead-free double perovskite has garnered considerable attention [15–29]. Several double perovskites have been synthesized experimentally [16–21], while most of them are less attractive for solar cells because of the undesired indirect or large band gaps. Meanwhile, theoretical materials screening for efficient solar cell absorbers in the double perovskites have been studied [22–26]. It has been analyzed that to achieve the electronic and optical properties comparable to the lead halide perovskite the most suitable replacement is by the combination of In as the M^+ cation and Bi or Sb as the M^{3+} cation, since they all have fully occupied s^2 states analogous to Pb^{2+} [5,22,27,28]. $\text{Cs}_2\text{InBiCl}_6$ and $\text{Cs}_2\text{InSbCl}_6$ are proposed as high-performance solar absorbers due to the suitable direct band gap, small effective masses, and small exciton binding energies [22], but they confront with the instability problem caused by the spontaneous oxidation of In^+ into In^{3+} [29]. Very recently, Volonakis *et al.* have found that the oxidation of In^+ into In^{3+} becomes energetically less favorable as the size of the A-site cation increases, suggesting that the In^+ -based halide double perovskites may be stabilized using a large organic molecule such as CH_3NH_3 or $\text{CH}(\text{NH}_2)_2$ as the A-site cation instead of all inorganic ions [28]. Their attention mainly focused on the organic-inorganic hybrid halide double perovskite $(\text{CH}_3\text{NH}_3)_2\text{InBiBr}_6$ in the orthorhombic phase, while particular attention should also be paid to the stability

*xhuang@njupt.edu.cn

†yangzhihong@njupt.edu.cn

and optoelectronic properties of In⁺-containing double perovskites in other phase structures, as well as other halogen elements (i.e., I or Cl) as X-site anions, which have not yet been explored.

In this paper, we will explore the stability, electronic, and optical properties of the lead-free halide double perovskites (CH₃NH₃)₂InBiX₆ (X = I, Br, Cl) using first-principles calculations. The orthorhombic, tetragonal, and cubic structures for each compound are considered in the calculations. From the viewpoint of thermodynamic stability, the decomposition energies against the possible competitive phases and *ab initio* molecular dynamic (AIMD) simulations at room temperature are investigated. Particularly, the effects of hydrostatic pressure on the decomposition energies are studied. It is shown that the decomposition energies increase under a small magnitude of hydrostatic pressure, implying the improved thermodynamic stability. Finally, we calculate the electronic and optical properties for the double perovskites and discuss implications of our results from the viewpoint of photovoltaic properties. The results reveal the potential prospect of (CH₃NH₃)₂InBiX₆ (X = I, Br, Cl) double perovskites as efficient solar cell absorbers.

II. COMPUTATION DETAILS AND CRYSTAL STRUCTURES

The density functional theory calculations are conducted using the projector-augmented wave method as implemented in VASP [30,31]. The generalized gradient approximation with Perdew-Burke-Ernzerhof (PBE) potentials is used for geometry optimizations and total-energy calculations in all compounds, including double perovskites and possible secondary phases [32,33]. The plane-wave cutoff energy is set to 500 eV, a Γ -centered k -point grid of $4 \times 3 \times 4$ is used for the orthorhombic phase, and a $4 \times 4 \times 3$ grid is used for both the tetragonal and the cubic phase. The lattice parameters and atomic positions are fully relaxed until the Hellmann-Feynman forces on each atom become less than 0.01 eV/Å. To accurately describe the electronic structures of double perovskites, the Heyd-Scuseria-Ernzerhof (HSE) hybrid functional with spin-orbit coupling (SOC) is utilized during band-structure calculations [34,35]. The latter is carried out by considering the investigated compounds to contain heavy element Bi. The electron and hole effective masses are calculated by the finite difference method using the equation $m^* = \hbar^2 / (\partial^2 \varepsilon(k) / \partial k^2)$, where $\varepsilon(k)$ are the band-edge eigenvalues and k is the wave vector [36]. AIMD simulations based on only the Γ point are performed to explore the thermal stability of the double perovskites at room temperature. The Nosé algorithm is employed to manipulate the temperature and the total dynamic steps are set up to 6000 steps with a time step of 1.0 fs. The optical absorption spectra of double perovskites are calculated according to the energy-dependent dielectric function [37]: $\varepsilon(\omega) = \varepsilon_1(\omega) + i\varepsilon_2(\omega)$, where $\varepsilon_1(\omega)$ and $\varepsilon_2(\omega)$ are the real and imaginary parts of the dielectric function, respectively. Based on $\varepsilon_1(\omega)$ and $\varepsilon_2(\omega)$, the optical absorption coefficient $\alpha(\omega)$ can be calculated by the following formula [38]:

$$\alpha(\omega) = \sqrt{2} \frac{\omega}{c} \left[\sqrt{\varepsilon_1^2(\omega) + \varepsilon_2^2(\omega)} - \varepsilon_1(\omega) \right]^{1/2}. \quad (1)$$

The PBE+SOC plus scissor operator is adopted for calculations of optical absorption spectra. That is, the optical absorption spectra from the PBE+SOC calculations are corrected by the scissor operator to match the corresponding HSE+SOC band-gap values. The used number of empty bands is threefold the number of occupied bands.

A schematic crystal structure of hybrid halide double perovskites (CH₃NH₃)₂InBiX₆ (X = I, Br, Cl) is shown in Fig. 1(a). It can be seen that the InX₆ and BiX₆ octahedra alternate in every direction, forming rocksalt-type ordering, as this rocksalt sublattice has been reported to be the ground state for most oxide double perovskites [39]. The dipolar organic methylammonium ions (CH₃NH₃) are located in the octahedra cages. To explore the properties of hypothetical double perovskites (CH₃NH₃)₂InBiX₆ (X = I, Br, Cl), structural data of typical lead halide perovskite CH₃NH₃PbI₃ are used to construct the structures. Note that CH₃NH₃PbI₃ possesses three typical crystal structures: (i) orthorhombic phase (*Pnma*) at low temperature, (ii) tetragonal phase (*I4/mcm*) at room temperature, and (iii) cubic phase (*Pm $\bar{3}$ m*) at high temperature ($T > 330$ K) [40]. Therefore, double perovskites in orthorhombic, tetragonal, and cubic phases are also all considered in our calculations [Figs. 1(b)–1(e)].

For both tetragonal [Fig. 1(d)] and orthorhombic [Fig. 1(e)] phases, we start from the tetragonal and orthorhombic phases of CH₃NH₃PbI₃, and then replace the four Pb atoms in the unit cell with In and Bi, maintaining the rocksalt ordering with 48 atoms per unit cell. For the cubic phase, the $\sqrt{2} \times \sqrt{2} \times 2$ cubic CH₃NH₃PbI₃ supercell is first constructed to ensure that the number of total atoms in the cubic phase is equal to those in orthorhombic and tetragonal phase. The same approach is then adopted to replace Pb atoms by In and Bi to form double perovskites. As shown in Figs. 1(b) and 1(c), two different cubic structures with different polarization are obtained. An asymmetric charge distribution that exists within each CH₃NH₃ cation with the positive charge localized on the NH₃ group results in an uncompensated electric dipole moment oriented from the carbon to the nitrogen atom. The dipole moments of all CH₃NH₃ cations in Fig. 1(b) point in the same direction, leading to an artificial ferroelectric, while experimentally it has been shown that the CH₃NH₃ molecules are normally oriented randomly, causing the CH₃NH₃PbI₃ to be paraelectric [41–43]. In order to avoid this artificial ferroelectric, we assume that the dipole moments of the adjacent CH₃NH₃ molecules in the same layer point in opposite directions, thus the net dipole moment in the whole unit cell is compensated due to zero dipole moment at each layer. Hence, we denote these two different structures as “cubic polar” [Fig. 1(b)] and “cubic nonpolar” [Fig. 1(c)], respectively.

III. RESULTS AND DISCUSSION

A. Stability of (CH₃NH₃)₂InBiX₆ (X = I, Br, Cl)

Since we have considered four possible structures for each (CH₃NH₃)₂InBiX₆ (X = I, Br, Cl) double perovskite, the ground state for each compound is first determined by comparing the total energies (see Table I). The results show that the most energetically favorable structure for (CH₃NH₃)₂InBiI₆ is the orthorhombic form, and that for

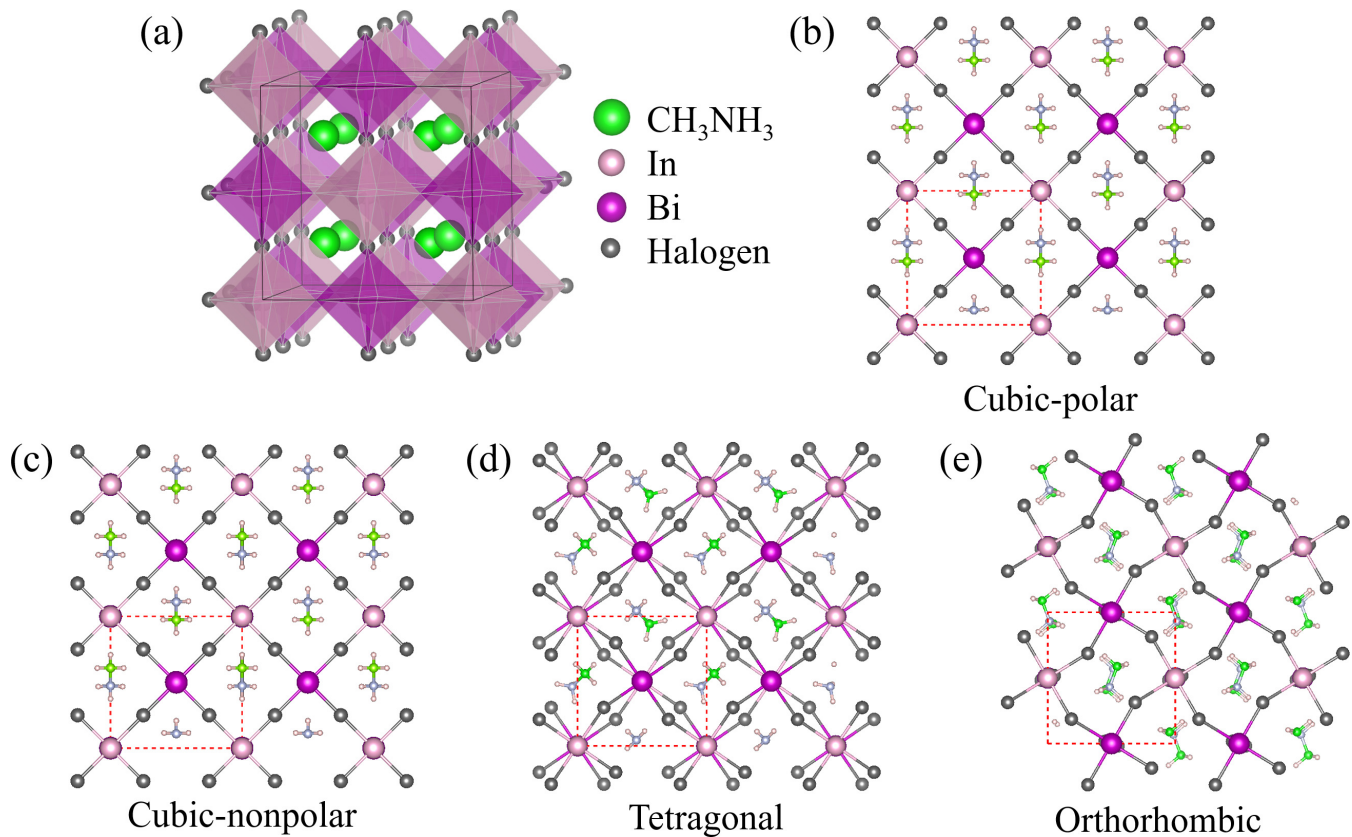


FIG. 1. The schematic crystal structure of (a) $(\text{CH}_3\text{NH}_3)_2\text{InBiX}_6$ ($X = \text{halogen}$) hybrid halide double perovskites in four different phases, which are (b) cubic polar, (c) cubic nonpolar, (d) tetragonal, and (e) orthorhombic. The red dashed squares in (b)–(e) indicate the unit cells and the green and light blue balls in (b)–(e) indicate carbon and nitrogen atoms, respectively.

both $(\text{CH}_3\text{NH}_3)_2\text{InBiBr}_6$ and $(\text{CH}_3\text{NH}_3)_2\text{InBiCl}_6$ it is the tetragonal form, while the energy differences between the orthorhombic and tetragonal form for all compounds are small, within 3 meV/atom, indicating that these compounds should adopt either orthorhombic or tetragonal structure if they can be synthesized. Here, below, we focus on the properties of the most energetically favorable structure for each compound.

Then, we examine the thermodynamic stabilities of the $(\text{CH}_3\text{NH}_3)_2\text{InBiX}_6$ ($X = \text{I, Br, Cl}$) double perovskites by calculating the decomposition energies against the related competitive phases. It has been demonstrated that the oxidation-reduction (redox) mechanism of In in the $A_2\text{InBiX}_6$ double perovskites is important [29]. Therefore, in our calculations, not only the elemental, binary and Bi-based $A_3\text{Bi}_2X_9$ ternary phases are considered as the possible decomposition products, but also the oxidized In^{3+} -based $A_3\text{In}_2X_9$ ternary products (see Table II). We construct the structure of $(\text{CH}_3\text{NH}_3)_3\text{Bi}_2X_9$ based on the experimentally reported crystal data [44,45]

and make the assumption that $(\text{CH}_3\text{NH}_3)_3\text{In}_2X_9$ compounds have the same structure as $\text{Cs}_3\text{In}_2\text{Br}_9$ [46]. Specifically, six different decomposition pathways have been calculated (see Table II), and the relevant decomposition energies (ΔH_d) are defined as the energy difference between the decomposition products and the $(\text{CH}_3\text{NH}_3)_2\text{InBiX}_6$ double perovskites. Here, a positive value of ΔH_d represents energy increased from the decomposed products to the $(\text{CH}_3\text{NH}_3)_2\text{InBiX}_6$ double perovskites, reflecting thermodynamically stable double perovskites. The larger the ΔH_d value, the more stable.

Figure 2(a) illustrates the calculated decomposition energies of the $(\text{CH}_3\text{NH}_3)_2\text{InBiX}_6$ ($X = \text{I, Br, Cl}$) double perovskites along three representative decomposition pathways. In Fig. 2(a), the pink bars correspond to the most typical nonredox decompositions into only binary products; those inorganic halide double perovskites are usually synthesized via its inverse reaction [19–21]. The blue bars correspond to the lowest ΔH_d nonredox decomposition pathways involving

TABLE I. The calculated energy difference ΔE (in units of meV/atom) between the four different structures for $(\text{CH}_3\text{NH}_3)_2\text{InBiX}_6$ ($X = \text{I, Br, Cl}$) double perovskites. The ground-state energy is set as reference energy zero.

ΔE	Cubic nonpolar	Cubic polar	Orthorhombic	Tetragonal
$(\text{CH}_3\text{NH}_3)_2\text{InBiI}_6$	1.8	4.1	0	1.6
$(\text{CH}_3\text{NH}_3)_2\text{InBiBr}_6$	4.2	2.3	1.9	0
$(\text{CH}_3\text{NH}_3)_2\text{InBiCl}_6$	4.6	2.6	2.2	0

TABLE II. The crystal structures and calculated total energies E_{total} at 0 GPa for double perovskites $(\text{CH}_3\text{NH}_3)_2\text{InBiX}_6$ ($X = \text{I}, \text{Br}, \text{Cl}$) and possible secondary phases. All results are calculated with the PBE pseudopotential. The decomposition pathways considered in our calculations are listed in the bottom of the table.

Formula	E_{total} (eV/formula)	Formula	E_{total} (eV/formula)
Bi ($R-3m$)	-3.874	$\text{CH}_3\text{NH}_3\text{Br}$ ($P21/m$)	-42.942
InI ($Cmcm$)	-5.048	$\text{CH}_3\text{NH}_3\text{Cl}$ ($Pbcm$)	-43.454
InBr ($Cmcm$)	-5.577	$(\text{CH}_3\text{NH}_3)_3\text{Bi}_2\text{I}_9$ ($P6_3/mmc$)	-148.006
InCl ($P2_13$)	-6.069	$(\text{CH}_3\text{NH}_3)_3\text{Bi}_2\text{Br}_9$ ($P-3m1$)	-152.962
InI_3 ($P2_1/c$)	-9.136	$(\text{CH}_3\text{NH}_3)_3\text{Bi}_2\text{Cl}_9$ ($P-3m1$)	-157.870
InBr_3 ($C2/m$)	-10.857	$(\text{CH}_3\text{NH}_3)_3\text{In}_2\text{I}_9$ ($P6_3/mmc$)	-145.741
InCl_3 ($P6_3/mmc$)	-12.040	$(\text{CH}_3\text{NH}_3)_3\text{In}_2\text{Br}_9$ ($P6_3/mmc$)	-150.991
BiI_3 ($R-3$)	-10.391	$(\text{CH}_3\text{NH}_3)_3\text{In}_2\text{Cl}_9$ ($P6_3/mmc$)	-156.108
BiBr_3 ($P2_1/c$)	-11.900	$(\text{CH}_3\text{NH}_3)_2\text{InBiI}_6$	-100.297
BiCl_3 ($Pnma$)	-13.166	$(\text{CH}_3\text{NH}_3)_2\text{InBiBr}_6$	-103.735
$\text{CH}_3\text{NH}_3\text{I}$ ($P21/m$)	-42.339	$(\text{CH}_3\text{NH}_3)_2\text{InBiCl}_6$	-106.965
$(\text{CH}_3\text{NH}_3)_2\text{InBiX}_6 \rightarrow 2\text{CH}_3\text{NH}_3\text{X} + \text{InX} + \text{BiX}_3$			
$(\text{CH}_3\text{NH}_3)_2\text{InBiX}_6 \rightarrow 2\text{CH}_3\text{NH}_3\text{X} + \text{InX}_3 + 1/3\text{BiX}_3 + 2/3\text{Bi}$			
$(\text{CH}_3\text{NH}_3)_2\text{InBiX}_6 \rightarrow 1/2\text{CH}_3\text{NH}_3\text{X} + 1/2(\text{CH}_3\text{NH}_3)_3\text{Bi}_2\text{X}_9 + \text{InX}$			
$(\text{CH}_3\text{NH}_3)_2\text{InBiX}_6 \rightarrow 3/2\text{CH}_3\text{NH}_3\text{X} + 1/6(\text{CH}_3\text{NH}_3)_3\text{Bi}_2\text{X}_9 + \text{InX}_3 + 2/3\text{Bi}$			
$(\text{CH}_3\text{NH}_3)_2\text{InBiX}_6 \rightarrow 1/2(\text{CH}_3\text{NH}_3)_3\text{In}_2\text{X}_9 + 1/2\text{CH}_3\text{NH}_3\text{X} + 1/3\text{BiX}_3 + 2/3\text{Bi}$			
$(\text{CH}_3\text{NH}_3)_2\text{InBiX}_6 \rightarrow 1/2(\text{CH}_3\text{NH}_3)_3\text{In}_2\text{X}_9 + 1/6(\text{CH}_3\text{NH}_3)_3\text{Bi}_2\text{X}_9 + 2/3\text{Bi}$			

Bi-based ternary and In-based binary compounds, where In is in the +1 state. The green bars correspond to the lowest ΔH_d redox decompositions involving In-based ternary compounds such as $(\text{CH}_3\text{NH}_3)_3\text{In}_2\text{I}_9$, $(\text{CH}_3\text{NH}_3)_3\text{In}_2\text{Br}_9$, and $(\text{CH}_3\text{NH}_3)_3\text{In}_2\text{Cl}_9$, where In is in its +3 oxidation state. As compared with ΔH_d values for only-binary-product decompositions (see pink bars), those values are largely decreased when the ternary products are involved, especially under the redox decompositions (see green bars). Fortunately, all of the double perovskites show positive ΔH_d values for the considered decomposition pathways. $(\text{CH}_3\text{NH}_3)_2\text{InBiCl}_6$ exhibits the smallest ΔH_d value of 0.69 meV/atom under the redox decomposition, which is in close proximity to the stable boundary. However, recall that the same case for $\text{Cs}_2\text{InBiCl}_6$ is about -16 meV/atom [29], implying that the thermodynamic stability of In^+ -based A_2InBiX_6 double perovskites is indeed improved when the CH_3NH_3 molecule is used as the A-site cation.

Next, we explore whether the thermodynamic stability of the $(\text{CH}_3\text{NH}_3)_2\text{InBiX}_6$ double perovskites could be further improved. Hydrostatic pressure has recently emerged as an effective means to tune the structural and photovoltaic properties for the lead halide perovskites [47] and lead-free halide double perovskites [48]. As an attempt, we investigate the effects of hydrostatic pressure on the decomposition energies. In detail, for the all $(\text{CH}_3\text{NH}_3)_2\text{InBiX}_6$ double perovskites and related secondary phases, the lattice structures are first fully relaxed under different pressure, and the total energies at the corresponding pressure are then calculated using the above optimized structures. Lastly, the ΔH_d values at different pressures are obtained, as shown in Figs. 2(b)–2(d). As the hydrostatic pressure increases, the decomposition energies for all double perovskites exhibit general trends of increasing first, followed by a decrease. In the relatively small pressure region from 0 to 4 GPa, almost all of the ΔH_d values are increased, implying the thermodynamic stability is enhanced

against decomposition. Particularly, for the redox decomposition at 4 GPa [Fig. 2(d)], the ΔH_d values are increased to 23.7, 14.6, and 9.6 meV/atom for $(\text{CH}_3\text{NH}_3)_2\text{InBiX}_6$ ($X = \text{I}, \text{Br}, \text{Cl}$), respectively. In general, most $\text{A}_2\text{M}^+\text{M}^{3+}\text{X}_6$ ($A =$ inorganic ion) double perovskites demonstrate good stability with fairly large positive values of ΔH_d above 20 meV/atom. Thus, $(\text{CH}_3\text{NH}_3)_2\text{InBiI}_6$ is now within a good thermodynamically stable region, and the thermodynamic stabilities for $(\text{CH}_3\text{NH}_3)_2\text{InBiBr}_6$ and $(\text{CH}_3\text{NH}_3)_2\text{InBiCl}_6$ are both improved. On the other side, in the relatively large pressure region from 6 to 10 GPa, the ΔH_d values are sharply decreased, implying the thermodynamic stability is largely reduced. For instance, for $(\text{CH}_3\text{NH}_3)_2\text{InBiBr}_6$ at 10 GPa, ΔH_d values even become negative, indicating it may spontaneously decompose even if synthesized. Accordingly, we propose that the application of a small magnitude of hydrostatic pressure should be beneficial for the stabilization of $(\text{CH}_3\text{NH}_3)_2\text{InBiX}_6$ double perovskites.

In addition, it is very important to verify whether the $(\text{CH}_3\text{NH}_3)_2\text{InBiX}_6$ ($X = \text{I}, \text{Br}, \text{Cl}$) double perovskites are stable at room temperature. Thus, AIMD simulations are conducted to explore the thermal stability of the structures under the condition of 300 K. During our AIMD simulations, the lattice parameters remain unchanged and the chemical bonds are not broken. Figure 3 presents the fluctuations of total energy and temperature as a function of simulation time at 300 K. It is clearly seen that when the temperature fluctuates strongly [Figs. 3(a)–3(c)] the total energy still oscillates within a very narrow range [Figs. 3(d)–3(f)], suggesting that $(\text{CH}_3\text{NH}_3)_2\text{InBiX}_6$ double perovskites can survive at room temperature.

B. Electronic structures of $(\text{CH}_3\text{NH}_3)_2\text{InBiX}_6$ ($X = \text{I}, \text{Br}, \text{Cl}$)

Figures 4(a)–4(c) show the calculated electronic band structures for the $(\text{CH}_3\text{NH}_3)_2\text{InBiX}_6$ ($X = \text{I}, \text{Br}, \text{Cl}$)

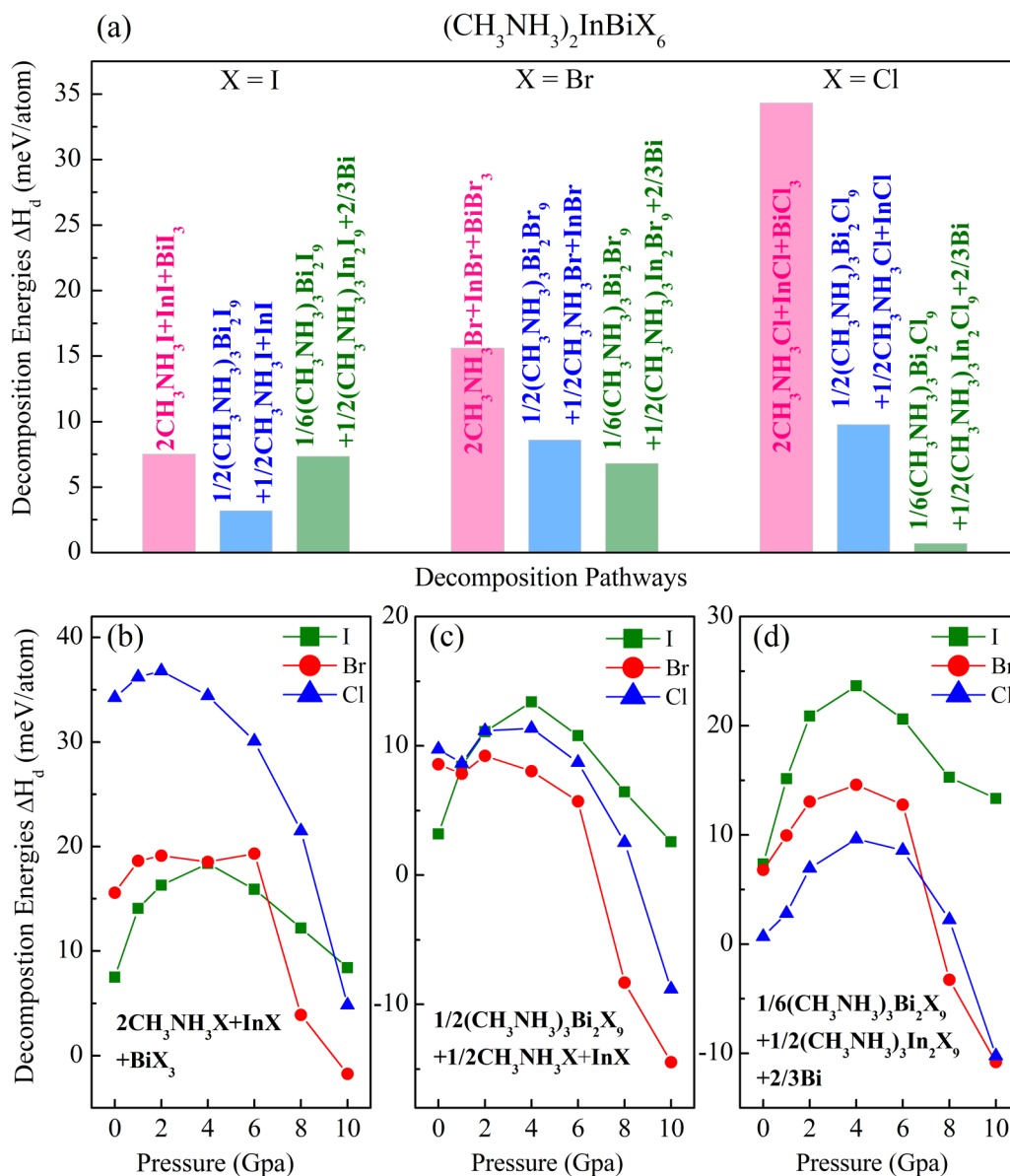


FIG. 2. (a) Calculated decomposition energies ΔH_d of $(\text{CH}_3\text{NH}_3)_2\text{InBiX}_6$ (X = I, Br, Cl) double perovskites along three representative decomposition pathways. The pink bars indicate pathways involving only binary compounds. The blue and green bars indicate the lowest ΔH_d nonredox and redox pathways involving ternary compounds. (b–d) Calculated decomposition energies ΔH_d of $(\text{CH}_3\text{NH}_3)_2\text{InBiX}_6$ (X = I, Br, Cl) double perovskites as a function of hydrostatic pressure for the three decomposition pathways considered in (a).

double perovskites by the HSE+SOC method. First, $(\text{CH}_3\text{NH}_3)_2\text{InBiX}_6$ (X = I, Br, Cl) double perovskites all exhibit direct band gaps at the Γ point, which is favorable for producing strong absorbance in photovoltaic materials. This band feature could be clarified by analyzing the constituents for band-edge states. As a representative example, the atom-projected density of states of $(\text{CH}_3\text{NH}_3)_2\text{InBiBr}_6$ is shown in Fig. 4(d). It should be noted that generally neither the A-site nor the X-site elements in the $\text{A}_2\text{M}^+\text{M}^{3+}\text{X}_6$ compounds modify the direct/indirect nature of the fundamental gap, but depend on the M^+ and M^{3+} cations (e.g., In^+ and Bi^{3+} here). In other words, the orbital constituents at the band edges for $(\text{CH}_3\text{NH}_3)_2\text{InBiI}_6$ and $(\text{CH}_3\text{NH}_3)_2\text{InBiCl}_6$ are similar with the case in $(\text{CH}_3\text{NH}_3)_2\text{InBiBr}_6$, except in terms of the energy

positions of hybridized In/Bi/halogen states. As seen from Fig. 4(d), the conduction-band minimum (CBM) is mainly composed of antibonding states of Bi-6p and Br-4p orbitals with a minor contribution of In-5p states. The valence-band maximum (VBM) is mainly composed of antibonding states of In-5s and Br-4p orbitals with a minor contribution of Bi-6s states. This orbital constituents at the band edge are analogous to those of APbX_3 perovskite, with Pb p states at the CBM and Pb s states at the VBM. Hence, orbital matching between In-5s and Bi-6s and the consequent completely symmetric p-s hybridization with the bromide atoms would result in the VBM at the Γ point, and the direct band gap finally. Additionally, In/Bi has similar contribution to the CBM and VBM, leading to a 3D connectivity of atomic orbitals. This reveals

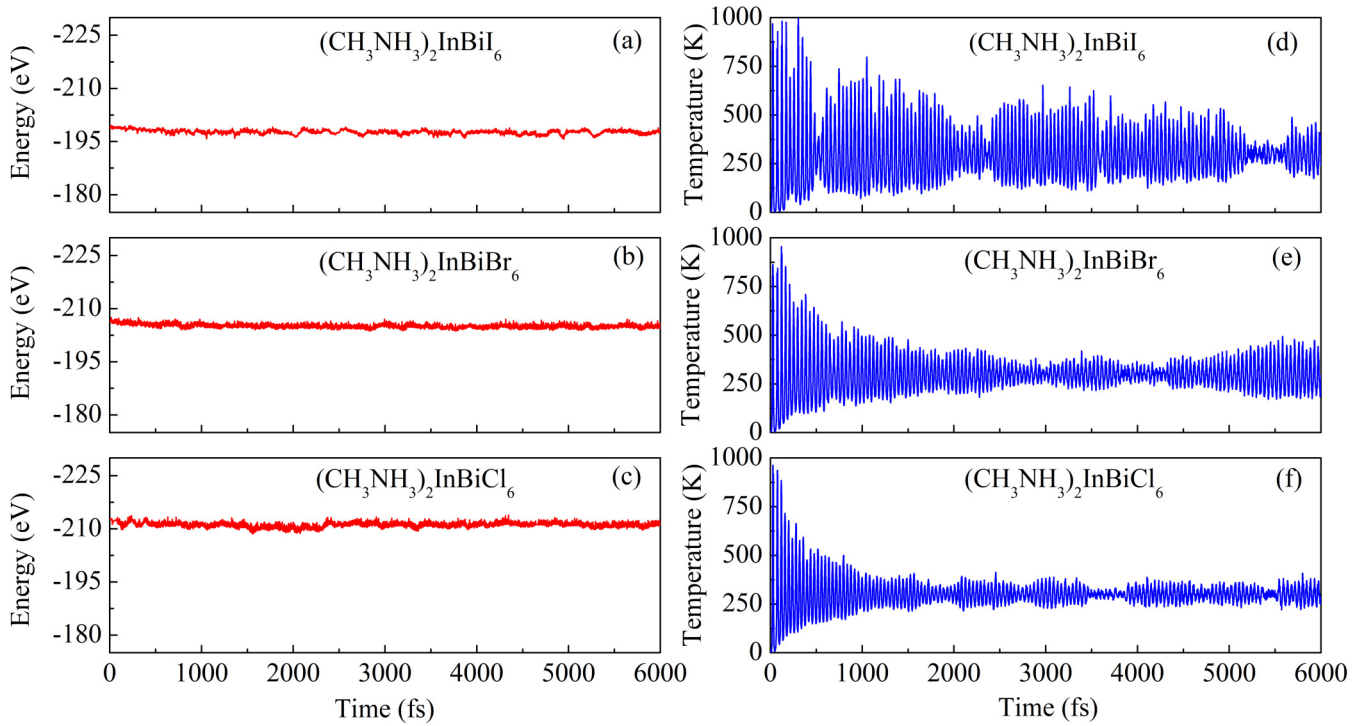


FIG. 3. Fluctuation of (a–c) total energy and (d–f) temperature as a function of testing time in AIMD at 300 K for $(\text{CH}_3\text{NH}_3)_2\text{InBiX}_6$ ($X = \text{I, Br, Cl}$) double perovskites.

electronically 3D character of $(\text{CH}_3\text{NH}_3)_2\text{InBiX}_6$ double perovskites, which is preferred for obtaining high photovoltaic performance.

Second, due to the strong $s - p/p - p$ orbital hybridization in the valence/conduction bands along with 3D electronic dimensionality, both the VBM and CBM exhibit large band dispersion. This corresponds to quite small effective masses for hole and electron [e.g., $0.34/0.31m_e$ for $(\text{CH}_3\text{NH}_3)_2\text{InBiCl}_6$, $0.18/0.19m_e$ for $(\text{CH}_3\text{NH}_3)_2\text{InBiBr}_6$, and $0.16/0.17m_e$ for $(\text{CH}_3\text{NH}_3)_2\text{InBiI}_6$ with SOC effect], which are good for carrier extraction. Moreover, we would like to mention that the SOC effect has a notable effect on our calculated effective masses of the VBM and CBM states. When excluding SOC effect, the calculated effective masses for hole and electron are $0.36/1.2m_e$ for $(\text{CH}_3\text{NH}_3)_2\text{InBiCl}_6$, $0.28/0.9m_e$ for $(\text{CH}_3\text{NH}_3)_2\text{InBiBr}_6$, and $0.16/0.6m_e$ for $(\text{CH}_3\text{NH}_3)_2\text{InBiI}_6$, respectively. The SOC effect significantly reduces the calculated effective masses especially for the electron masses; the reduction is about 75%. This striking reduction is also noticed in lead halide perovskites, in which the electron masses can be reduced by nearly one order of magnitude when SOC effect is considered [49].

Finally, we observe that the band gap narrows with the halogen atom moving from Cl to Br to I, which are 1.66 eV for $(\text{CH}_3\text{NH}_3)_2\text{InBiCl}_6$, 1.02 eV for $(\text{CH}_3\text{NH}_3)_2\text{InBiBr}_6$, and 0.77 eV for $(\text{CH}_3\text{NH}_3)_2\text{InBiI}_6$, respectively [see the black arrows in Figs. 4(a)–4(c)]. The trend of the band gap is dominated by the increase of CBM bandwidth moving from Cl (0.56 eV) to Br (0.67 eV) to I (1.08 eV). Since delocalization in the p orbital increases from Cl-3 p to Br-4 p to I-5 p , the more delocalized X - p orbitals overlap more with the Bi-6 p

wave functions, resulting in more dispersive conduction bands and the downshift of the CBM, thus exhibiting a smaller band gap. This band feature also implies that the halogen at the X site can be used to modulate the band gap, in agreement with previous experiments about lead halide perovskites [50,51]. Significantly, these hypothetic organic-inorganic hybrid double perovskites, especially $(\text{CH}_3\text{NH}_3)_2\text{InBiBr}_6$ and $(\text{CH}_3\text{NH}_3)_2\text{InBiCl}_6$, possess suitable band gaps for photovoltaic application, larger than that of reported inorganic InBi-based double perovskites [e.g., $\text{Cs}_2\text{InBiI}_6$ (0.21 eV), $\text{Cs}_2\text{InBiBr}_6$ (0.33 eV), and $\text{Cs}_2\text{InBiCl}_6$ (0.88 eV)] [29]. We recall that the larger A -site cation normally makes the 3D perovskite network more distorted as well as the octahedral, and tends to drive the system to exhibit a larger band gap, consistent with the case in $(\text{Cs}/\text{CH}_3\text{NH}_3/\text{CH}_2(\text{NH}_2)_2)\text{PbI}_3$ [52–54]. Consequently, the $(\text{CH}_3\text{NH}_3)_2\text{InBiX}_6$ double perovskites have electronic band structures quite similar to the APbX_3 perovskite, and thus should display favorable optical absorption properties.

C. Optical properties of $(\text{CH}_3\text{NH}_3)_2\text{InBiX}_6$ ($X = \text{I, Br, Cl}$)

Figure 5 presents the optical absorption spectra of $(\text{CH}_3\text{NH}_3)_2\text{InBiX}_6$ ($X = \text{I, Br, Cl}$) double perovskites, calculated by the PBE+SOC method along with the scissor operator. Additionally, the absorption spectra of GaAs and $\text{CH}_3\text{NH}_3\text{PbI}_3$ are also shown for comparison. First, for $(\text{CH}_3\text{NH}_3)_2\text{InBiX}_6$ double perovskites, we see that the shapes of the three absorption curves are similar, whereas the spectrum is redshifted as the halogen atom moves from Cl to Br to I, in agreement with the trend of the band gap discussed above.

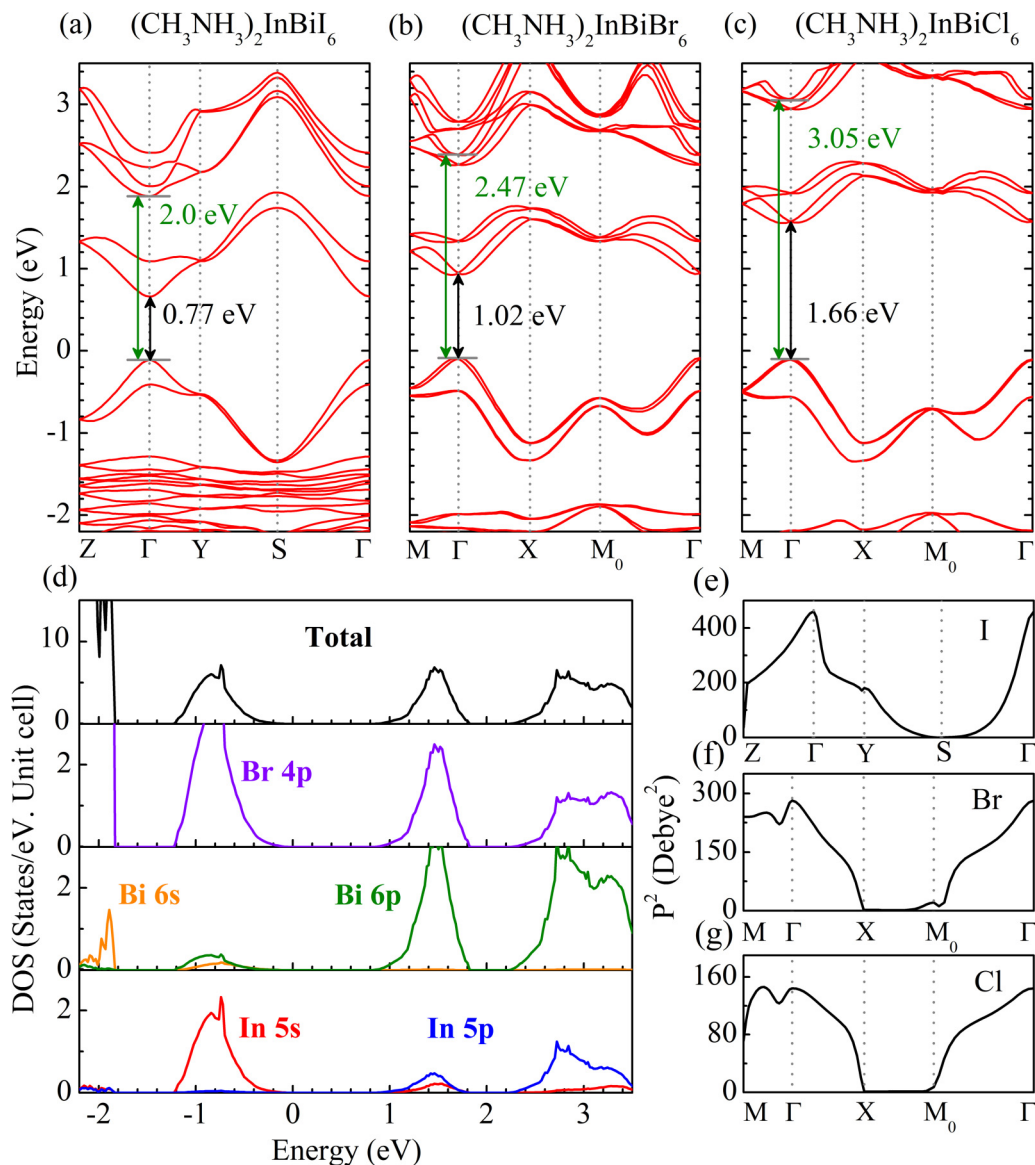


FIG. 4. Calculated band structures and corresponding dipole transition matrix elements (in arbitrary units) for (a), (e) $(\text{CH}_3\text{NH}_3)_2\text{InBiI}_6$, (b), (f) $(\text{CH}_3\text{NH}_3)_2\text{InBiBr}_6$, and (c), (g) $(\text{CH}_3\text{NH}_3)_2\text{InBiCl}_6$. (d) Total and projected densities of states for $(\text{CH}_3\text{NH}_3)_2\text{InBiBr}_6$.

Second, both $(\text{CH}_3\text{NH}_3)_2\text{InBiI}_6$ and $(\text{CH}_3\text{NH}_3)_2\text{InBiBr}_6$ exhibit strong optical absorption throughout the visible-light range ($\approx 10^3 \text{ cm}^{-1}$), which is comparable to $\text{CH}_3\text{NH}_3\text{PbI}_3$ in the *Pnma* phase (orange curve in Fig. 5), while the optical absorption coefficient of $(\text{CH}_3\text{NH}_3)_2\text{InBiCl}_6$ reaches up to 10^5 cm^{-1} only in the blue- and purple-light range with higher photon energy, which is comparable with traditional film solar cell absorber GaAs (magenta curve in Fig. 5). In detail, $(\text{CH}_3\text{NH}_3)_2\text{InBiI}_6$ (red curve in Fig. 5) shows a higher optical absorption coefficient than $(\text{CH}_3\text{NH}_3)_2\text{InBiBr}_6$ (green curve in Fig. 5) and $(\text{CH}_3\text{NH}_3)_2\text{InBiCl}_6$ (blue curve in Fig. 5), as also evidenced by the results of calculated dipole transition matrix elements [see Figs. 4(e)–4(g)]. The sum of the squares of the dipole transition matrix elements P^2 reveals the transition probabilities between the topmost valence and the lowest conduction band. The higher value of P^2 , the higher transition probability and the stronger optical absorption. It is noted that $(\text{CH}_3\text{NH}_3)_2\text{InBiI}_6$ [Fig. 4(e)] has a much larger value of P^2 at

the Γ point as compared with $(\text{CH}_3\text{NH}_3)_2\text{InBiBr}_6$ [Fig. 4(f)] and $(\text{CH}_3\text{NH}_3)_2\text{InBiCl}_6$ [Fig. 4(g)].

Another important characteristic for efficient photovoltaic materials is a sharp absorption edge. We display the optical absorption coefficient curves using a logarithmic scale, allowing for easy identification of the absorption onset. For $(\text{CH}_3\text{NH}_3)_2\text{InBiX}_6$ ($X = \text{I}, \text{Br}, \text{Cl}$), their absorption coefficient curves all exhibit sharp onsets, as the energy range for the absorption coefficient to rise to 10^4 cm^{-1} is only about 0.2 eV, which is comparable with $\text{CH}_3\text{NH}_3\text{PbI}_3$. Additionally, their absorption onsets are at photon energies of 0.77, 1.02, and 1.66 eV, respectively, which match well with their corresponding calculated electronic band gaps, suggesting the excitations from the VBM to the CBM at the Γ point. Then, the optical absorption coefficients start to rise steadily and the obvious absorption peaks appear at about 2.0 eV for $(\text{CH}_3\text{NH}_3)_2\text{InBiI}_6$, 2.47 eV for $(\text{CH}_3\text{NH}_3)_2\text{InBiBr}_6$, and 3.05 eV for $(\text{CH}_3\text{NH}_3)_2\text{InBiCl}_6$. Later, the optical

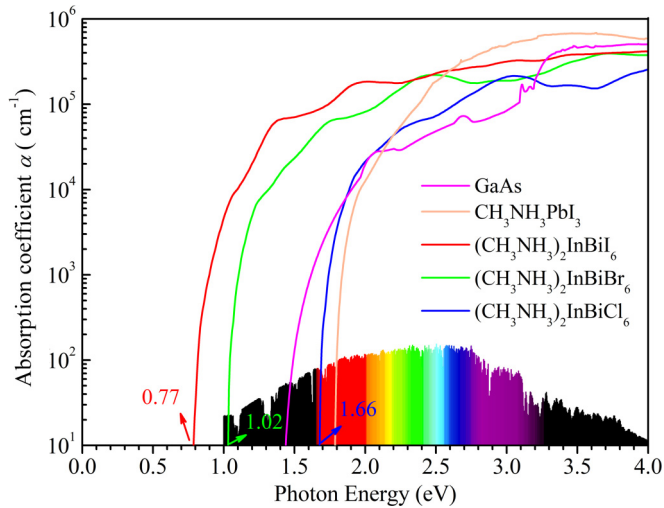


FIG. 5. Calculated optical absorption spectra of $(\text{CH}_3\text{NH}_3)_2\text{InBiX}_6$ ($X = \text{I}, \text{Br}, \text{Cl}$) double perovskites. The results of GaAs and $\text{CH}_3\text{NH}_3\text{PbI}_3$ are shown for comparison. The standard AM1.5G solar spectrum is shown on the bottom as a reference with different colors from red to purple indicating the visible light spectrum.

absorption coefficients continue increasing at higher photon energies. It is known that the absorption peaks beyond the absorption onset are attributed to the interband dipole transitions. Through measuring the interband gap, it is found that the interband gaps between the VBM and the higher conduction band at the Γ point [see the green arrows in Figs. 4(a)–4(c)] exactly coincide with the specified photon energies of the above-mentioned absorption peaks, implying the dipole transitions from hybrid halogen- $p/\text{In-}5s$ states at the VBM to hybrid halogen- $p/\text{In-}5p/\text{Bi-}6p$ states at the conduction bands. We emphasize the Γ point here, because the dipole transition matrix element decreases strongly as the k point moves from Γ to other high-symmetry points for all three compounds [see Figs. 4(e)–4(g)]. Therefore, the direct band-gap p - p optical transition from halogen- p to $\text{In}/\text{Bi-}p$

orbitals in $(\text{CH}_3\text{NH}_3)_2\text{InBiX}_6$ double perovskites could result in strong optical absorptions, which is also an important reason for excellent optical absorptions in the lead halide perovskites [8].

IV. CONCLUSION

In summary, we have presented a detailed study of the stability, electronic, and optical properties of $(\text{CH}_3\text{NH}_3)_2\text{InBiX}_6$ ($X = \text{I}, \text{Br}, \text{Cl}$) double perovskites. Our results indicate that the $(\text{CH}_3\text{NH}_3)_2\text{InBiX}_6$ ($X = \text{I}, \text{Br}, \text{Cl}$) double perovskites are thermodynamically stable; especially the $(\text{CH}_3\text{NH}_3)_2\text{InBiCl}_6$ is within a good thermodynamically stable region. In addition, the decomposition energies against the possible secondary phases show an increasing trend under a small magnitude of hydrostatic pressure, implying that the application of hydrostatic pressure may improve the thermodynamic stability of In^+ -based halide double perovskites. The calculated electronic band structures for $(\text{CH}_3\text{NH}_3)_2\text{InBiX}_6$ ($X = \text{I}, \text{Br}, \text{Cl}$) double perovskites exhibit suitable direct band gaps, small carrier effective masses for both electrons and holes, together with 3D electronic dimensionalities. This, in turn, results in strong optical absorptions. Both electronic and optical features would make $(\text{CH}_3\text{NH}_3)_2\text{InBiX}_6$ ($X = \text{I}, \text{Br}, \text{Cl}$) double perovskites suitable for photovoltaics and optoelectronics. We therefore hope that our theoretical studies will stimulate more further experimental efforts in the In^+ -based lead-free halide double perovskites.

ACKNOWLEDGMENTS

This work is supported by the National Natural Science Foundation of China (Grants No. 11804165 and No. 11804169), the Natural Science Foundation of the Jiangsu Higher Education Institutions of China (Grants No. 18KJB140011 and No. 18KJB140009), and the Natural Science Foundation of Jiangsu Province (Grant No. BK20180741). This work is also supported by Nanjing University of Posts and Telecommunications (Grant No. NY218133).

- [1] Best Research-Cell Efficiencies (NREL, 2020), <https://www.nrel.gov/pv/assets/pdfs/best-research-cell-efficiencies.20200128.pdf>.
- [2] L. Mazzarella, Y.-H. Lin, S. Kirner, A. B. Morales-Vilches, L. Korte, S. Albrecht, E. Crossland, B. Stannowski, C. Case, H. J. Snaith, and R. Schlattmann, *Adv. Energy Mater.* **9**, 1803241 (2019).
- [3] Z. Xiao, W. Meng, J. Wang, D. B. Mitzi, and Y. Yan, *Mater. Horiz.* **4**, 206 (2017).
- [4] F. Giustino and H. J. Snaith, *ACE Energy Lett.* **1**, 1233 (2016).
- [5] X.-G. Zhao, D. Yang, J.-C. Ren, Y. Sun, Z. Xiao, and L. Zhang, *Joule* **2**, 1662 (2018).
- [6] W. Ning and F. Gao, *Adv. Mater.* **31**, 1900326 (2019).
- [7] D. Yang, J. Lv, X.-G. Zhao, Q. Xu, Y. Fu, Y. Zhan, A. Zunger, and L. Zhang, *Chem. Mater.* **29**, 524 (2017).
- [8] W.-J. Yin, T. Shi, and Y. Yan, *Adv. Mater.* **26**, 4653 (2014).
- [9] Z. Xiao and Y. Yan, *Adv. Energy Mater.* **7**, 1701136 (2017).
- [10] N. K. Noel, S. D. Stranks, A. Abate, C. Wehrenfennig, S. Guarnera, A. A. Haghighirad, A. Sadhanala, G. E. Eperon, S. K. Pathak, M. B. Johnston, A. M. Petrozza, L. M. Herz, and H. J. Snaith, *Energy Environ. Sci.* **7**, 3061 (2014).
- [11] F. Hao, C. C. Stoumpos, D. H. Cao, R. P. Chang, and M. G. Kanatzidis, *Nat. Photonics* **8**, 489 (2014).
- [12] B.-W. Park, B. Philippe, X. Zhang, H. Rensmo, G. Boschloo, and E. M. J. Johansson, *Adv. Mater.* **27**, 6806 (2015).
- [13] J.-C. Hebig, I. Kühn, J. Flohre, and T. Kirchartz, *ACS Energy Lett.* **1**, 309 (2016).
- [14] P. C. Harikesh, H. K. Mulmudi, B. Ghosh, T. W. Goh, Y. T. Teng, K. Thirumal, M. Lockrey, K. Weber, T. M. Koh, S. Li, S. Mhaisalkar, and N. Mathews, *Chem. Mater.* **28**, 7496 (2016).
- [15] G. Volonakis, M. R. Filip, A. A. Haghighirad, N. Sakai, B. Wenger, H. J. Snaith, and F. Giustino, *J. Phys. Chem. Lett.* **7**, 1254 (2016).

- [16] G. Volonakis, A. A. Haghighirad, R. L. Milot, W. H. Sio, M. R. Filip, B. Wenger, M. B. Johnston, L. M. Herz, H. J. Snaith, and F. Giustino, *J. Phys. Chem. Lett.* **8**, 772 (2017).
- [17] L. Chu, W. Ahmad, W. Liu, J. Yang, R. Zhang, Y. Sun, J. Yang, and X. A. Li, *Nano-Micro Lett.* **11**, 16 (2019).
- [18] F. Wei, Z. Deng, S. Sun, F. Zhang, D. M. Evans, G. Kieslich, S. Tominaka, M. A. Carpenter, J. Zhang, P. D. Bristowe, and A. K. Cheetham, *Chem. Mater* **29**, 1089 (2017).
- [19] A. H. Slavney, T. Hu, A. M. Lindenberg, and H. I. Karunadasa, *J. Am. Chem. Soc.* **138**, 2138 (2016).
- [20] E. T. McClure, M. R. Ball, W. Windl, and P. M. Woodward, *Chem. Mater.* **28**, 1348 (2016).
- [21] F. Wei, Z. Deng, S. Sun, F. Xie, G. Kieslich, D. M. Evans, M. A. Carpenter, P. Bristowe, and T. Cheetham, *Mater. Horiz.* **3**, 328 (2016).
- [22] X.-G. Zhao, J.-H. Yang, Y. Fu, D. Yang, Q. Xu, L. Y. S.-H. Wei, and L. Zhang, *J. Am. Chem. Soc.* **139**, 2630 (2017).
- [23] W. Meng, X. Wang, Z. Xiao, J. Wang, D. B. Mitzi, and Y. Yan, *J. Phys. Chem. Lett.* **8**, 2999 (2017).
- [24] X.-G. Zhao, D. Yang, Y. Sun, T. Li, L. Zhang, L. Yu, and A. Zunger, *J. Am. Chem. Soc.* **139**, 6718 (2017).
- [25] Z. Deng, F. Wei, S. Sun, G. Kieslich, A. K. Cheetham, and P. D. Bristowe, *J. Mater. Chem. A* **4**, 12025 (2016).
- [26] M. R. Filip, X. Liu, A. Miglio, G. Hautier, and F. Giustino, *J. Phys. Chem. C* **122**, 158 (2018).
- [27] C. N. Savory, A. Walsh, and D. O. Scanlon, *ACS Energy Lett.* **1**, 949 (2016).
- [28] G. Volonakis, A. A. Haghighirad, H. J. Snaith, and F. Giustino, *J. Phys. Chem. Lett.* **8**, 3917 (2017).
- [29] Z. Xiao, K.-Z. Du, W. Meng, J. Wang, D. B. Mitzi, and Y. Yan, *J. Am. Chem. Soc.* **139**, 6054 (2017).
- [30] G. Kresse and J. Furthmüller, *Phys. Rev. B* **54**, 11169 (1996).
- [31] G. Kresse and J. Hafner, *Phys. Rev. B* **47**, 558(R) (1993).
- [32] P. E. Blöchl, *Phys. Rev. B* **50**, 17953 (1994).
- [33] J. P. Perdew, K. Burke, and M. Ernzerhof, *Phys. Rev. Lett.* **77**, 3865 (1996).
- [34] J. Heyd, G. E. Scuseria, and M. Ernzerhof, *J. Chem. Phys.* **118**, 8207 (2003).
- [35] J. Heyd, G. E. Scuseria, and M. Ernzerhof, *J. Chem. Phys.* **124**, 219906 (2006).
- [36] L. D. Whalley, J. M. Frost, B. J. Morgan, and A. Walsh, *Phys. Rev. B* **99**, 085207 (2019).
- [37] M. Gajdoš, K. Hummer, G. Kresse, J. Furthmüller, and F. Bechstedt, *Phys. Rev. B* **73**, 045112 (2006).
- [38] X. Huang, T. R. Paudel, S. Dong, and E. Y. Tsymbal, *Phys. Rev. B* **92**, 125201 (2015).
- [39] S. Vasala and M. Karppinen, *Prog. Solid State Chem.* **43**, 1 (2015).
- [40] T. Baikie, Y. Fang, J. M. Kadro, M. Schreyer, F. Wei, S. G. Mhaisalkar, M. Graetzel, and T. J. White, *J. Mater. Chem. A* **1**, 5628 (2013).
- [41] A. M. A. Leguy, J. M. Frost, A. P. McMahon, V. G. Sakai, W. Kockelmann, C. Law, X. Li, F. Foglia, A. Walsh, B. C. O'Regan, J. Nelson, J. T. Cabral, and P. R. F. Barnes, *Nat. Commun.* **6**, 7124 (2015).
- [42] A. A. Bakulin, O. Selig, H. J. Bakker, Y. L.A. Rezus, C. Müller, T. Glaser, R. Lovrincic, Z. Sun, Z. Chen, A. Walsh, J. M. Frost, and T. L. C. Jansen, *J. Phys. Chem. Lett.* **6**, 3663 (2015).
- [43] Q. Xu, A. Stroppa, J. Lv, X.-G. Zhao, D. Yang, K. Biswas, and L. Zhang, *Phys. Rev. Mater.* **3**, 125401 (2019).
- [44] M. E. Kamminga, A. Stroppa, S. Picozzi, M. Chislov, I. A. Zvereva, J. Baas, A. Meetsma, G. R. Blake, and T. T. Palstra, *Inorg. Chem.* **56**, 33 (2017).
- [45] M. Leng, Z. Chen, Y. Yang, Z. Li, K. Zeng, K. Li, G. Niu, Y. He, Q. Zhou, and J. Tang, *Angew. Chem.* **128**, 15236 (2016).
- [46] G. Z. Meyer, *Anorg. Allg. Chem.* **445**, 140 (1978).
- [47] G. Liu, L. Kong, W. Yang, and H.-K. Mao, *Mater. Today* **27**, 91 (2019).
- [48] Q. Li, Y. Wang, W. Pan, W. Yang, B. Zou, J. Tang, and Z. Quan, *Angew. Chem., Int. Ed.* **56**, 15969 (2017).
- [49] W. Gao, X. Gao, T. A. Abtew, Y.-Y. Sun, S. Zhang, and P. Zhang, *Phys. Rev. B* **93**, 085202 (2016).
- [50] J. H. Noh, S. H. Im, J. H. Heo, T. N. Mandal, and S. I. Seok, *Nano Lett.* **13**, 1764 (2013).
- [51] J. S. Bechtel and A. V. D. Ven, *Phys. Rev. Mater.* **2**, 045401 (2018).
- [52] M. R. Filip, G. E. Eperon, H. J. Snaith, and F. Giustino, *Nature Commun.* **5**, 5757 (2014).
- [53] D. P. McMeekin, G. Sadoughi, W. Rehman, G. E. Eperon, M. Saliba, M. T. Hörantner, A. Haghighirad, N. Sakai, L. Korte, B. Rech, M. B. Johnston, L. M. Herz, and H. J. Snaith, *Science* **351**, 151 (2016).
- [54] G. E. Eperon, T. Leijtens, K. A. Bush, R. Prasanna, T. Green, Jacob T.-W. Wang, D. P. McMeekin, G. Volonakis, R. L. Milot, R. May, A. Palmstrom, D. J. Slotcavage, R. A. Belisle, J. B. Patel, E. S. Parrott, R. J. Sutton, W. Ma, F. Moghadam, B. Conings, A. Babayigit, H.-G. Boyen, S. Bent, F. Giustino, L. M. Herz, M. B. Johnston, M. D. McGehee, and H. J. Snaith, *Science* **354**, 861 (2016).